PHYSICAL REVIEW B **77**, 024106 (2008)

Giant magnetoelectric effect induced by intrinsic surface stress in ferroic nanorods

M. D. Glinchuk,[1] E. A. Eliseev,[1] A. N. Morozovska,[1,*] and R. Blinc[2]
[1]*Institute for Problems of Materials Science, NAS of Ukraine, Krjijanovskogo 3, 03142 Kiev, Ukraine*
[2]*Jozef Stefan Institute, P.O. Box 3000, 1001 Ljubljana, Slovenia*

(Received 25 September 2007; revised manuscript received 7 November 2007; published 16 January 2008)

The general approach for the consideration of the magnetoelectric effects in ferroic nanorods is proposed in the framework of the phenomenological theory. The intrinsic surface stress, magneto- and electrostriction, as well as piezoelectric and piezomagnetic effects are included in the free energy. The intrinsic surface stress under the curved nanoparticle surface is shown to play an important role in the shift of ferroelectric and ferromagnetic transition temperatures and appearance of built-in magnetic and electric fields, which are inversely proportional to the nanorod radius. We consider the case of quadratic and linear magnetoelectric coupling coefficients. The linear coupling coefficient is radius independent, whereas the quadratic ones include terms inversely proportional to the nanorod radius and thus strongly increase with radius decrease. We predicted that quadratic magnetoelectric coupling induces dielectric tunability increase by 2–50 times in the vicinity of ferromagnetic and ferroelectric phase transition points. The quadratic magnetoelectric coupling dramatically changes the phase diagrams of ferroic nanorods under their radius decrease. In particular, the second order phase transition may become the first one. Special attention is paid to the case when polarization, magnetization, and magnetoelectric couplings are induced by intrinsic surface stress in nanorods.

DOI: 10.1103/PhysRevB.77.024106 PACS number(s): 77.80.−e, 77.84.Dy, 68.03.Cd, 68.35.Gy

I. INTRODUCTION

The magnetoelectric (ME) effect, i.e., when the application of either a magnetic field or an electric field induces an electric polarization as well as magnetization, attracted much attention in the last few years.[1] Although it was predicted by Curie[2] in 1894 on the basis of symmetry consideration and first observed in 1961 in an antiferromagnetic Cr_2O_3 crystal,[3] the observed ME effect was small (about a few percent) that retarded its broad investigation and especially technical applications. The latter is related to the fact that ME materials must exhibit high ME coefficients for such important applications as magnetoelectric sensors in radio electronics, optoelectronics, microwave electronics, transducers, and magnetically tuned capacitors, etc. Recently, the revival of the ME effect has been observed due to the discovery of high (several hundred percent) ME effects both in single-phase and composite materials (see Refs. 4–7 and review Ref. 8, and references therein). Most of the composites exhibit a high extrinsic ME effect resulting from the interaction between magnetic and electric components via, e.g., their magnetostriction and piezoelectric properties, as well as piezomagnetic-piezoelectric interaction.[9–12] Physical reasons of the high ME effect are still unclear in single-phase materials, where the ME effect is intrinsic (see, e.g., Ref. 13). The description of this effect in microscopic theory based on a Hamiltonian with spin-orbit interaction frequently uses the idea that spin current symmetry belongs to the same class as the electric polarization and so it is natural to expect coupling between them.[14,15] However, here, one could hardly expect a high ME coefficient.

The phenomenological theory approach for the description of ME effect obligatory uses the interaction of magnetization and electric polarization with mechanical tension both in composites[9,16] and single-phase materials.[17,18] However, no indication on the possibility to obtain high ME coupling was revealed for the conventional type of mechanical conditions in the single phase bulk materials.

The probability to obtain high ME coupling would appear when mechanical conditions become completely different under the confinement of nanomaterials. Some evidence in favor of this assumption follows from the observation of dramatically higher ME coefficients in epitaxially (001) oriented $BiFeO_3$ films on a $SrTiO_3$ substrate than in the bulk crystals. This effect was suggested to be related to the influence of boundary conditions in the consideration performed in Ref. 19. The authors of Ref. 19 came to the conclusion that ME effect and other properties might be understood in terms of the appearance of a homogeneously magnetized state in the film. Such a striking phenomenon as the observation of ferromagnetism in spherical nanoparticles (size 7−30 nm) of nonmagnetic oxides such as CeO_2, Al_2O_3, ZnO, etc., has been recently reported in Ref. 20. Extremely strong superparamagnetic behavior down to 4 K has been found in gold and palladium nanoparticles with mean diameter of 2.5 nm and narrow size distribution with no magnetization in bulk.[21] The appearance of ferroelectricity takes place in nanorods and films of the incipient ferroelectrics, which remain para-electric up to 0 K in bulk.[22,23] It was shown in the papers that the possible physical origin of electrical polarization and magnetization could be mechanical conditions in the restricted geometry of nanomaterials and, in particular, the influence of intrinsic surface stress. Therefore, it is not excluded that new secondary ferroics with **M** and **P** might appear among oxide nanomaterials. This type of secondary ferroic is known to be a possibility for obtaining high ME effects.[8] However, up to now, no calculations were performed to find out if the restricted geometry and related mechanical boundary conditions could influence the value of ME effect coefficients. In this paper, we performed such calculations. We applied a phenomenological theory approach for oxide materials in the form of nanorods. Below, we present the details of our model.

The paper is organized as follows. Section II includes the most general form of free energy including striction, piezocoefficients, and ME linear and nonlinear interaction. Order parameters M and P are obtained after minimization of free energy with respect to stress components (Sec. II B). Sections III and IV consider built-in electric and magnetic fields and ME coupling coefficient size effect calculations. The consideration of size effects on the phase diagrams, electric and magnetoelectric susceptibilities, as well as dielectric tunability in the external magnetic field can be found in Sec. IV. In the last section, we consider the most widely spread case of nonzero quadratic ME effect only, to show that even in this case, size effects become very strong.

II. THEORETICAL APPROACH

A. Model of calculations

We will consider the secondary ferroics with two order parameters, magnetization $\mathbf{M}$ and electric polarization $\mathbf{P}$. These order parameters can be either inherent in the bulk material or induced by confinements of nanorods. Keeping in mind that ferromagnetism has been observed at room temperature in nanoparticles of 7–30 nm size[20] and the sizes about 50 nm are suitable for the appearance of ferroelectricity,[22] we consider nanorods with the sizes of 5–50 nm. For such small sizes, the influence of surface and related boundary conditions including surface tension are known to be high. Thus, the properties are expected to be more close to those near the surface than those in the bulk. While for larger sizes, e.g., more than 100 nm, the properties are known to change gradually from those on the surface to those in the bulk (see, e.g., Refs. 24 and 25) for the considered sizes less than 50 nm, the properties can be regarded as homogeneous and under the strong influence of surface tension. The main mechanism of the mechanical tension relaxation is known to be misfit dislocations, but the considered nanorod sizes are usually smaller than the critical size Δh_d of dislocation appearance;[26] thus, the properties can be considered homogeneous. As a matter of fact, such approach is in agreement with the so-called shell and core model of nanoparticles,[27] where the core is the inner part of a particle that does not "feel" the influence of surface contrary to the shell (outer part). The core properties are practically the same as those in the bulk. Investigation of ferroelectric nanoparticles by electron-spin-resonance method had shown[28] that the shell sizes are in the region from several to tens of nanometers. The characteristic feature of the shell is the absence of spatial inversion symmetry and so the existence of piezoelectric effect even for cubic symmetry in the bulk. In the general case, one can also suggest the existence of piezomagnetic effect. In what follows, we will consider long cylindrical nanorods with electrical polarization along the z axis and magnetization along one of three equivalent axes with external electric and magnetic fields along the z and x directions correspondingly (see Fig. 1). The nanorods are clamped and long enough ($h \gg R$), so for the considered geometry, depolarization field is absent. Also, it is possible to make the demagnetization field negligible.[29] Under such conditions, single domain state will be the most preferable. Electro- and magnetostriction effects as well as mechanical stress tensor with boundary conditions at the curved nanoparticle surface must be taken into account. We assume that nanorods are well separated from one another and do not interact electrically or magnetically.

B. Gibbs energy renormalization caused by intrinsic surface stresses

Let us consider a rather long cylindrical ferroic nanorod with free sidewalls ($\rho = R$) clamped between the wafer ($z = -h/2$) and top electrode ($z = +h/2$) (see Fig. 1).

In what follows, we will use one set of parameters for the nanoparticle. Such a situation is possible for a nanorod of small radius. However, it is not excluded that numerical values and the symmetry of material tensorial constants differ from the ones tabulated for the bulk material, e.g., there are "shell" constants intergrown through the nanoparticle "core." For this important case, several electro- and/or magnetomechanical coupling phenomena absent in the bulk may appear from the symmetry breaking in the vicinity of surface (see below).

Let us assume that polarization is directed along the polar axis z and magnetization along the weak magnetic anisotropy axis x, i.e., $\mathbf{P} = (0, 0, P_3)$ and $\mathbf{M} = (M_1, 0, 0)$. So, the Gibbs energy expansion of the homogeneous polarization $P_3(T)$, magnetization $M_1(T)$, and stress σ_{ij} has the form

$$\begin{aligned} G_R = 2\pi h \int_0^R \rho d\rho \Bigg\{ & a_1 P_3^2 + a_{11} P_3^4 + a_{111} P_3^6 - [Q_{11}\sigma_{33} \\ & + Q_{12}(\sigma_{11} + \sigma_{22})]P_3^2 - \frac{1}{2}(A_{11}\sigma_{11}^2 + A_{11}\sigma_{22}^2 + A_{33}\sigma_{33}^2)P_3^2 \\ & + \cdots - g^e_{3jk}\sigma_{jk}P_3 + b_1 M_1^2 + b_{11} M_1^4 + a_{111} M_1^6 - [Z_{11}\sigma_{33} \\ & + Z_{12}(\sigma_{11} + \sigma_{22})]M_1^2 - \frac{1}{2}(B_{11}\sigma_{11}^2 + B_{11}\sigma_{22}^2 + B_{33}\sigma_{33}^2)M_1^2 \\ & + \cdots - g^m_{1jk}\sigma_{jk}M_1 - \frac{1}{2}s_{11}(\sigma_{11}^2 + \sigma_{22}^2 + \sigma_{33}^2) \\ & - s_{12}(\sigma_{11}\sigma_{22} + \sigma_{11}\sigma_{33} + \sigma_{33}\sigma_{22}) - \frac{1}{2}s_{44}(\sigma_{23}^2 + \sigma_{13}^2 + \sigma_{12}^2) \\ & + f_{ijkl}\sigma_{ij}^2\sigma_{kl}^2 - M_1 H_0 - P_3 E_0 \Bigg\}. \end{aligned} \tag{1}$$

Subscripts 1, 2, and 3 denote Cartesian coordinates x, y, and z, respectively; we use Voigt notation or matrix notation when necessary ($xx = 1$, $yy = 2$, $zz = 3$, $zy = 4$, $zx = 5$, $xy = 6$). Coefficients $a_1(T)$ and $b_1(T)$ explicitly depend on temperature T in the framework of the Landau-Ginzburg approach. All higher order expansion coefficients are regarded temperature independent. Since we assume that the order parameters and elastic stress spatial distribution are homogeneous inside the nanorod, we should neglect the gradient energy. Note that for the film on the substrate, this assumption is valid when the film thickness is less than the critical thickness of misfit dislocation appearance that is known to be dozens of nanometers.[26]

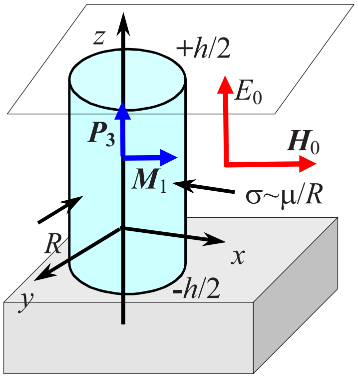

FIG. 1. (Color online) Geometry of cylindrical particle. x is one of the three equivalent weak magnetic anisotropy axes; z is the polar ferroelectric axis. The external electric field E_0 is directed along the polar axes; magnetic field H_0 is directed along the x axis. The geometry $H_0 \perp E_0$ is typical for the majority of experiments.

In Eq. (1), Q_{ij} and Z_{ij} are, respectively, the electro- and magnetostriction tensor coefficients; s_{ij} are components of the elastic compliance tensor.[30] Hereinafter, we assume the symmetry of piezoelectric (g^e_{3jk}) and piezomagnetic (g^m_{3jk}) effects due to the fact that the surface influence is different from the cubic phase as follows: $g^e_{3jk}\sigma_{jk}P_3 = g^e_{31}(\sigma_{11}+\sigma_{22})P_3 + g^e_{33}\sigma_{33}P_3 + \cdots$ and $g^m_{1jk}\sigma_{jk}M_1 = g^m_{11}(\sigma_{11}+\sigma_{22})M_1 + g^m_{13}\sigma_{33}M_1 + \cdots$.

The distribution of stress σ_{ij} should satisfy the conditions of mechanical equilibrium as well as appropriate boundary conditions at the curved nanoparticle surface,

$$\frac{\partial \sigma_{ij}}{\partial x_i} = 0,$$

$$\sigma_{\rho\rho}\big|_{\rho=R} = -\frac{\mu}{R}, \qquad \sigma_{\rho\varphi}\big|_{\rho=R} = 0, \qquad \sigma_{\rho z}\big|_{\rho=R} = 0,$$

$$u_3(z = \pm h/2) = 0. \tag{2}$$

Here, $\mu_{ij} = \mu\delta_{ij}$ is the intrinsic surface stress tensor coefficient [31,32] which has nontrivial components only on the nanorod surface. The surface stress μ is strongly dependent on the ambient material.

Minimization of the free energy [Eq. (1)] with respect to the stress components σ_{ij} leads to the equations of state $\partial G_R / \partial \sigma_{ij} = -u_{ij}$, where u_{ij} are strain tensor components. Neglecting the terms $\sim f_{ijkl}\sigma^2_{ij}\sigma^2_{kl}$, one obtains that the homogeneous solution for the stress and strain tensor components σ_{ij} in Cartesian coordinates has the form

$$\sigma_{11} = \sigma_{22} = -\frac{\mu}{R}, \qquad \sigma_{12} = \sigma_{13} = \sigma_{23} = 0, \tag{3}$$

$$\sigma_{33} = \frac{s_{12}(2\mu/R) - Q_{11}P_3^2 - Z_{11}M_1^2 - g^e_{33}P_3 - g^m_{13}M_1}{s_{11} + A_{33}P_3^2 + B_{33}M_1^2}. \tag{4}$$

Rigorously speaking, solutions (3) and (4) are valid for nanorods of radius R less than the critical thickness Δh_d of surface stress relaxation (e.g., dislocation appearance[26]). For the case $R \lesssim \Delta h_d$, a rather complex inhomogeneous elastic problem with elastic stress and polarization gradients should be considered, which is far beyond the scope of the paper. An approximate solution could be obtained within the framework of the conventional core and shell model.[25] Elastic stress σ_{ij} given by Eqs. (3) and (4) is mainly concentrated in the shell region, whereas the core is almost unstressed (i.e., $\sigma_{ij} \approx 0$).

Typically, $\Delta h_d \sim 5-50$ nm. In what follows, we thus mainly consider the case $R < \Delta h_d$ (i.e., all the particles are in the shell region) since it is the most interesting one for surface and size effect manifestation. Effects related with the shell influence on the dielectric and magnetoelectric properties of thick nanorods will be qualitatively considered in the discussion.

Note that the considered mechanical boundary conditions represent one of the possible experimental situations. Performed calculations have shown that magnetoelectric coupling is absent in mechanically free rods, while in the case of partial clamping, the results are qualitatively similar to the ones considered below.

Hereinafter, we assume that the terms $A_{ii}\sigma^2_{ii}P_3^2$ and $B_{ii}\sigma^2_{ii}M_1^2$ are small, so we neglect their higher powers. Substituting Eqs. (3) and (4) into Eq. (1), we obtain the Gibbs energy with renormalized coefficients,

$$\begin{aligned} G_R = 2\pi h \int_0^R \rho d\rho \{ & \alpha_1(T,R)P_3^2 + \alpha_{11}P_3^4 - P_3[E_0 + E_p(R)] \\ & + \beta_1(T,R)M_1^2 + \beta_{11}M_1^4 + M_1[H_0 + H_p(R)] \\ & + g_{ME}(P_3, M_1)\}. \end{aligned} \tag{5}$$

The renormalized coefficients before P_3^2 and M_1^2 in the free energy [Eq. (5)] have the form

$$\begin{aligned} \alpha_1(T,R) = a_1(T) + \frac{(g^e_{33})^2}{2s_{11}} + \frac{2\mu}{R}\left(Q_{12} - Q_{11}\frac{s_{12}}{s_{11}}\right) \\ - \frac{2\mu^2}{R^2}\left(A_{11} + A_{33}\frac{s_{12}^2}{s_{11}^2}\right), \end{aligned} \tag{6a}$$

$$\begin{aligned} \beta_1(T,R) = b_1(T) + \frac{(g^m_{13})^2}{2s_{11}} + \frac{2\mu}{R}\left(Z_{12} - Z_{11}\frac{s_{12}}{s_{11}}\right) \\ - \frac{2\mu^2}{R^2}\left(B_{11} + B_{33}\frac{s_{12}^2}{s_{11}^2}\right). \end{aligned} \tag{6b}$$

The internal "built-in" fields induced by the piezoelectric and piezomagnetic effects are introduced as

$$E_p(R) = \left(\frac{s_{12}}{s_{11}}g^e_{33} - g^e_{31}\right)\frac{4\mu}{R}, \quad H_p(R) = \left(\frac{s_{12}}{s_{11}}g^m_{13} - g^m_{11}\right)\frac{4\mu}{R}. \tag{7}$$

The nanorod magnetoelectric energy density is

$$g_{ME} = (\gamma_{11}M_1P_3 + \gamma_{12}M_1P_3^2 + \gamma_{21}M_1^2P_3 + \gamma_{22}M_1^2P_3^2). \tag{8}$$

Linear and quadratic magnetoelectric coupling coefficients in the magnetoelectric energy [Eq. (8)] are

$$\gamma_{11} = \frac{g^e_{33} g^m_{13}}{s_{11}}, \tag{9a}$$

$$\gamma_{12} = g^m_{13}\left(\frac{Q_{11}}{s_{11}} + \frac{2\mu}{R}\frac{s_{12}A_{33}}{s^2_{11}}\right), \quad \gamma_{21} = g^e_{33}\left(\frac{Z_{11}}{s_{11}} + \frac{2\mu}{R}\frac{s_{12}B_{33}}{s^2_{11}}\right), \tag{9b}$$

$$\gamma_{22} = \left[\frac{Q_{11}Z_{11}}{s_{11}} - \frac{A_{33}(g^m_{13})^2 + B_{33}(g^e_{33})^2}{2s^2_{11}} + \frac{2\mu}{R}\frac{s_{12}}{s^2_{11}}(Q_{11}B_{33} + Z_{11}A_{33}) + \frac{4\mu^2}{R^2}\frac{s^2_{12}}{s^3_{11}}B_{33}A_{33}\right]. \tag{9c}$$

Both piezoelectric and piezomagnetic coefficient nonzero values $g^e_{33} \neq 0$ and $g^m_{13} \neq 0$ are necessary to obtain the nonzero linear coupling coefficient $\gamma_{11} \neq 0$ that may be possible in some special cases. For instance, $g^m_{33} = 1.2 \times 10^{-8}$ Wb/N and $g^m_{13} = -5.8 \times 10^{-9}$ Wb/N in bulk Terfenol-D.[11] If piezoelectric coupling is absent in the bulk, it may appear inside the nanorod of radius $R \leqslant \Delta h_d$ (or the corresponding shell region for $R > \Delta h_d$), allowing for the symmetry breaking on the surface. The coefficient $\gamma_{22} \neq 0$ is nonzero for all magnetoelectric materials. Note that the last term in Eq. (9c) proportional to the product $B_{33}A_{33}$ would be neglected hereinafter.

For the case $R \gg \Delta h_d$, the core (i.e., bulk) magnetoelectric coupling coefficients are radius independent and the magnetoelectric energy coincides with the one of the laterally clamped bulk material,

$$g_{ME} \approx \frac{g^e_{33} g^m_{13}}{s_{11}} M_1 P_3 + g^m_{13}\frac{Q_{11}}{s_{11}} M_1 P^2_3 + g^e_{33}\frac{Z_{11}}{s_{11}} M^2_1 P_3 + \frac{Q_{11}Z_{11}}{s_{11}} M^2_1 P^2_3. \tag{10}$$

III. BUILT-IN FIELD THICKNESS DEPENDENCE

The built-in electric and magnetic field [Eq. (7)] dependencies on nanorod radius are shown in Fig. 2 for typical material parameters. It is clear from the log-log dependencies that built-in fields increase with radius decrease and could overcome bulk coercive field values E_C and H_C (see solid and dashed lines).

Built-in electric field leads to the horizontal shift of all hysteresis loops and electretlike state appearance in ferroelectric films with thickness less than the critical one. It facilitates the thin film self-polarization as predicted in Refs. 33 and 34. Besides trivial hysteresis loop horizontal shifts [see Figs. 2(c) and 2(d)], we predict ordering effects caused by built-in magnetic fields and the radius dependent $H_p(R)$ effect may induce ferromagnetism or irreversible magnetization in small nanorods absent in the bulk material. This is similar to the ferroelectricity in incipient ferroelectric nanorods[22] and electret state in ultrathin films.[34] Under the absence of external magnetic field, the built-in magnetic field smears magnetic, dielectric and magnetoelectric susceptibility temperature maxima, increases their values in the paramagnetic phase, and essentially increases the magnetoelectric tunability. Therefore, both electric and magnetic built-in fields originated from piezoeffects and surface stress in nanorods essentially influence the nanoparticle properties.

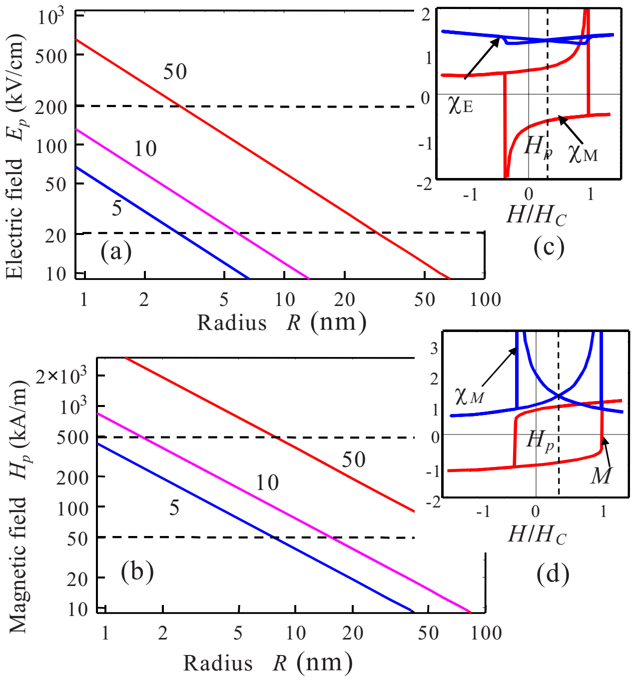

FIG. 2. (Color online) Built-in (a) electric and (b) magnetic field dependencies on nanorod radius for parameters $g^m_{13} \cong 10^{-9}$ Wb/N, $g^m_{11} = 0$, $g^e_{33} \cong 10^{-3}$V m/N, $g^e_{31} = 0$, $\mu = 5$, 10, and 50 N/m (figures near the curves), and $s_{12}/s_{11} = -0.3$. The region between the dashed lines corresponds to the typical range of bulk coercive fields E_C and H_C (see, e.g., Ref. 35). [(c) and (d)] Schematic hysteresis loops via the normalized magnetic field H/H_C. All values are normalized on their bulk values at zero fields without electromagnetic coupling. The electric field is assumed to be zero.

IV. SIZE EFFECT ON MAGNETOELECTRIC COUPLING COEFFICIENTS

Let us rewrite Eqs. (9a)–(9c) as

$$\gamma_{12}(R) = \gamma^b_{12}\left(1 + \frac{R_{12}}{R}\right), \quad \gamma_{21}(R) = \gamma^b_{21}\left(1 + \frac{R_{21}}{R}\right),$$

$$\gamma_{22}(R) \approx \gamma^b_{22}\left(1 + \frac{R_{22}}{R}\right), \tag{11}$$

where $\gamma^b_{12} = g^m_{13}(Q_{11}/s_{11})$, $R_{12} = 2\mu(s_{12}A_{33}/s_{11}Q_{11})$, $\gamma^b_{21} = g^e_{33}(Z_{11}/s_{11})$, $R_{21} = 2\mu(s_{12}B_{33}/s_{11}Z_{11})$, $\gamma^b_{22} = (Q_{11}Z_{11}/s_{11}) - [A_{33}(g^m_{13})^2 + B_{33}(g^e_{33})^2/2s^2_{11}]$, and $R_{22} = R_{12} + R_{21} = 2\mu[s_{12}(Q_{11}B_{33} + Z_{11}A_{33})/s_{11}Q_{11}Z_{11}]$. Usually bulk material magnetoelectric coupling constants γ^b_{ij} are small or identically zero depending on the material symmetry.

The linear coupling coefficient is radius independent, whereas the quadratic ones include terms inversely proportional to the nanorod radius. They thus strongly increase with radius decrease. Linear magnetoelectric coupling γ_{11} breaks the symmetries $P \to -P$ and $M \to -M$ as well as smears the transition point even at zero magnetic and electric fields. So, Eq. (11) allows the strong renormalization and even sign change of $\gamma_{ij \neq 11}$ caused by intrinsic surface stress since characteristic parameters R_{ij} could be positive or negative. In accordance with estimations made in Ref. 36, usually, 1 nm$\leqslant |R_{12}| \leqslant$50 nm and 5 nm$\leqslant |R_{21}| \leqslant$50 nm, and so their sum $|R_{22}| \leqslant$100 nm. Size dependence of the normalized coupling coefficients is shown in Fig. 3. It is clear from Fig. 3 that at small radii $R/|R_{ij}| \ll 1$, coefficients $\gamma_{ij\neq 11}$ are much greater than their bulk values $\gamma^b_{ij\neq 11}$.

In what follows, we demonstrate the effects related to magnetoelectric coupling coefficients $\gamma_{ij \neq 11}$ and their influence on ferromagnetic and ferroelectric transition temperatures and properties.

V. SIZE EFFECT OF PHASE DIAGRAMS, ORDER PARAMETER AND GENERALIZED SUSCEPTIBILITIES

A. Renormalized instability temperatures, order parameters, and susceptibilities calculations

Using renormalized coefficients [Eqs. (6)–(9)], one can rewrite the free energy [Eqs. (5) and (8)] density $\tilde{g}(R,T)$ as follows:

$$\begin{aligned}\tilde{g}(R,T) = [&\alpha_1 P_3^2 + \beta_1 M_1^2 + \alpha_{11} P_3^4 + \beta_{11} M_1^4 - (E_p + E_0) P_3 \\ &- (H_p + H_0) M_1 + \gamma_{11} M_1 P_3 + \gamma_{12} M_1 P_3^2 \\ &+ \gamma_{21} M_1^2 P_3 + \gamma_{22} M_1^2 P_3^2]. \end{aligned} \qquad (12)$$

The coefficients α_1 and β_1 are temperature and radius dependent in accordance with Eqs. (6a) and (6b). They can be rewritten as $\alpha_1 = \alpha_T[T - T_{ce}(R)]$ and $\beta_1 = \beta_T[T - T_{cm}(R)]$. The temperatures $T_{ce}(R)$ and $T_{cm}(R)$ which do not take into account ME effect are:

$$T_{ce}(R) = T^*_{ce} - \frac{1}{\alpha_T}\left(\frac{R_Q}{R} - \frac{\rho_A}{R^2}\right), \quad T^*_{ce} = T^b_{ce} + \frac{(g^e_{33})^2}{2 s_{11} \alpha_T},$$

$$R_Q = 2\mu\left(Q_{12} - Q_{11}\frac{s_{12}}{s_{11}}\right), \quad \rho_A = 2\mu^2\left(A_{11} + A_{33}\frac{s^2_{12}}{s^2_{11}}\right), \qquad (13a)$$

$$T_{cm}(R) = T^*_{cm} - \frac{1}{\beta_T}\left(\frac{R_Z}{R} - \frac{\rho_B}{R^2}\right), \quad T^*_{cm} = T^b_{cm} + \frac{(g^m_{13})^2}{2 s_{11} \beta_T},$$

$$R_Z = 2\mu\left(Z_{12} - Z_{11}\frac{s_{12}}{s_{11}}\right), \quad \rho_B = 2\mu^2\left(B_{11} + B_{33}\frac{s^2_{12}}{s^2_{11}}\right). \qquad (13b)$$

The temperatures $T_{ce}(R)$ and $T_{cm}(R)$ determine the corresponding paraphrase instability for the first order phase transitions or the ferroelectric and ferromagnetic phase transition points for the second order phase transitions.

Note that both signs of characteristic constants $R_{Q,Z}$ and $\rho_{A,B}$ are possible. Estimations[22] proved that the contribution of terms $\sim 1/R$ becomes essential at radii less than 5–50 nm at the reasonable values of surface stress tensor $|\mu| = 5-50$ N/m.[37] At positive characteristic constants, size-induced phase transition exists, while the temperature enhancement is possible at their negative values. The inequality $T^*_{cm}/T^*_{ce} < 1$ is typical for the majority of bulk multiferroic materials such as $\mathrm{BiFeO_3}$, $\mathrm{Pb(Fe,Nb)O_3}$, and $\mathrm{Eu(Ba,Ti)O_3}$.[17] However, it is not excluded that $T_{cm}(R)/T_{ce}(R) < 1$ for nanorods of definite radius R, allowing for the considered size effects. The case $T^b_{cm} = 0$, $T^b_{ce} = 0$ corresponds to the bulk material without ferroic properties.

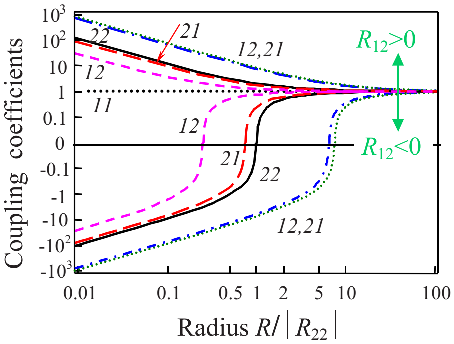

FIG. 3. (Color online) Size dependence of the normalized coupling coefficients $\tilde{\gamma}_{ij} = \gamma_{ij}/|\gamma^b_{ij}|$ via the nanorod radius $R/|R_{22}|$: $\tilde{\gamma}_{22}$ (solid curves, "22"), $\tilde{\gamma}_{12}$ ("12," long-dashed curves for $R_{12}/|R_{22}| = \pm 0.75$ and dotted curves for $R_{12}/|R_{22}| = \pm 7.5$), $\tilde{\gamma}_{12}$ ("21," short-dashed curves for $R_{12}/|R_{22}| = \pm 0.25$ and dash-dotted curves for $R_{12}/|R_{22}| = \pm 6.5$), and constant $\tilde{\gamma}_{11} = 1$ ("11," circles). To generate the plots, we used the identity $R_{21}/|R_{22}| = 1 - R_{12}/|R_{22}|$.

It is important for further consideration that characteristic parameters $R_{Q,Z}$ (as well as parameters $\rho_{A,B}$) [which determine the size-induced transition temperature shift in accordance with Eqs. (13a) and (13b)] and parameters R_{ij} [which determine the magnetoelectric coupling coefficient size effects in accordance with Eq. (11)] depend on the different material constants (e.g., piezoconstants), have different numerical values, and thus should be tuned independently.

The conditions of the free energy minimum, $\partial\tilde{g}/\partial P_3 = 0$ and $\partial\tilde{g}/\partial M_1 = 0$, lead to the coupled equations of state for the order parameter determination,

$$\begin{aligned}&2\alpha_1 P_3 + \gamma_{11} M_1 + 2\gamma_{12} M_1 P_3 + \gamma_{21} M_1^2 + 2\gamma_{22} P_3 M_1^2 + 4\alpha_{11} P_3^3 \\ &\quad = E_p + E_0,\end{aligned}$$

$$\begin{aligned}&2\beta_1 M_1 + \gamma_{11} P_3 + \gamma_{12} P_3^2 + 2\gamma_{21} M_1 P_3 + 2\gamma_{22} P_3^2 M_1 + 4\beta_{11} M_1^3 \\ &\quad = H_p + H_0.\end{aligned} \qquad (14)$$

After elementary transformations of Eq. (14) listed in Appendix B of Ref. 36, electric and magnetoelectric susceptibilities can be found as

$$\chi_E = \frac{\partial P_3}{\partial E_0} = \frac{2(\beta_1 + \gamma_{21} P_3 + \gamma_{22} P_3^2 + 6\beta_{11} M_1^2)}{\Delta(M_1, P_3)}, \qquad (15a)$$

TABLE I. The conditions of phase existence and stability in the absence of external fields.

Phase	Conditions
PP	$\alpha_1 > 0,\ \beta_1 > 0$
FE	$\alpha_1 < 0,\ \alpha_1\gamma_{22} - 2\beta_1\alpha_{11} < 0$
FM	$\beta_1 < 0,\ \beta_1\gamma_{22} - 2\alpha_1\beta_{11} < 0$
FEM	$\alpha_1\gamma_{22} - 2\beta_1\alpha_{11} > 0,\ \beta_1\gamma_{22} - 2\alpha_1\beta_{11} > 0,$ $4\alpha_{11}\beta_{11} - \gamma_{22}^2 > 0$ (secondary ferroic phase)

$$\chi_{ME} = \frac{\partial P_3}{\partial H_0} = \frac{\partial M_1}{\partial E_0} = -\frac{\gamma_{11} + 2\gamma_{12}P_3 + 2\gamma_{21}M_1 + 4\gamma_{22}M_1P_3}{\Delta(M_1,P_3)}, \tag{15b}$$

$$\chi_M = \frac{\partial M_1}{\partial H_0} = \frac{2(\alpha_1 + \gamma_{12}M_1 + \gamma_{22}M_1^2 + 6\alpha_{11}P_3^2)}{\Delta(M_1,P_3)}, \tag{15c}$$

where

$$\begin{aligned}\Delta(M_1,P_3) = [&4(\alpha_1 + \gamma_{12}M_1 + \gamma_{22}M_1^2 + 6\alpha_{11}P_3^2)\\ &\times(\beta_1 + \gamma_{21}P_3 + \gamma_{22}P_3^2 + 6\beta_{11}M_1^2)\\ &-(\gamma_{11} + 2\gamma_{12}P_3 + 2\gamma_{21}M_1 + 4\gamma_{22}M_1P_3)^2].\end{aligned} \tag{16}$$

Built-in fields [Eq. (7)] lead to the order parameter and susceptibility hysteresis loop horizontal shift, i.e., the loop horizontal scale is determined by the sum $H_p(R)+H_0$, as shown in Figs. 2(c) and 2(d).

Below, we mainly consider the most widely spread case of existence of the quadratic ME effect only (i.e., piezoeffect is absent and so $\gamma_{11}=0$, $\gamma_{12}=0$, $\gamma_{21}=0$, $\gamma_{22}\neq 0$, $H_p=E_p=0$, $T_{cm}^*=T_{cm}^b$, and $T_{ce}^*=T_{ce}^b$). Detailed consideration of the size-induced transition temperature shift will be presented in the next section, where we demonstrate that under the condition $\gamma_{22}(R) \gg |\gamma_{22}^b|$, the influence of the quadratic ME coupling term $\gamma_{22}M_1^2P_3^2$ on phase diagrams, susceptibilities, and order parameters becomes very strong.

B. Phase diagrams with magnetoelectric coupling, without external fields

For the case when magnetic and electric fields are absent ($H_0=0$, $E_0=0$), analysis of the free energy [Eq. (12)] is essentially simplified. In the Table I, we summarized general conditions for the stability and existence of the four different phases, namely, paraphase ($P=0$, $M=0$), ferroelectric ($P\neq 0$, $M=0$), ferromagnetic ($P=0$, $M\neq 0$), and mixed ferroelectric-ferromagnetic phase (secondary ferroic phase $P\neq 0$, $M\neq 0$) denoted as PP, FE, FM, and FEM, respectively.

Let us analyze essentially simplified Eqs. (14) and (15), which defined the polarization, magnetization, and susceptibilities. Keeping in mind that all these properties for FE and FM phases have a conventional form, we will concentrate our attention on the consideration of the FEM phase. In the considered case of nonzero quadratic ME effect only, Eq. (14) simplified to the form

$$\begin{gathered}2\alpha_1P_3 + 4\alpha_{11}P_3^3 + 2\gamma_{22}M_1^2P_3 = 0,\\ 2\beta_1M_1 + 4\beta_{11}M_1^3 + 2\gamma_{22}M_1P_3^2 = 0.\end{gathered} \tag{17}$$

It is easy to see from Eq. (17) that

$$\begin{gathered}P_{FEM}^2 = \frac{-2\alpha_1\beta_{11} + \beta_1\gamma_{22}}{4\alpha_{11}\beta_{11} - \gamma_{22}^2},\\ M_{FEM}^2 = \frac{-2\alpha_{11}\beta_1 + \alpha_1\gamma_{22}}{4\alpha_{11}\beta_{11} - \gamma_{22}^2}.\end{gathered} \tag{18}$$

This phase is stable at $-2\alpha_1\beta_{11}+\beta_1\gamma_{22}>0$, $-2\alpha_{11}\beta_1+\alpha_1\gamma_{22}>0$, and $4\alpha_{11}\beta_{11}-\gamma_{22}^2>0$ (see Table I). So, both numerator and denominator in Eq. (18) are positive for the FME phase.

Using the expressions [Eq. (18)] for P_{FEM}^2 and M_{FEM}^2, one can obtain that $\Delta(M_{FEM},P_{FEM})=16(4\alpha_{11}\beta_{11}-\gamma_{22}^2)P_{FEM}^2M_{FEM}^2$ and then rewrite Eqs. (15a)–(15c) as follows:

$$\chi_E = \frac{\beta_{11}}{2(-2\alpha_1\beta_{11} + \beta_1\gamma_{22})}, \tag{19}$$

$$\chi_M = \frac{\alpha_{11}}{2(-2\alpha_{11}\beta_1 + \alpha_1\gamma_{22})}, \tag{20}$$

$$\chi_{ME} = -\frac{\gamma_{22}}{4(4\alpha_{11}\beta_{11} - \gamma_{22}^2)M_{FEM}P_{FEM}} = \frac{\gamma_{22}}{2\sqrt{\beta_{11}\alpha_{11}}}\sqrt{\chi_E\chi_M}. \tag{21}$$

It is seen that in the points where P_{FEM}^2 or M_{FEM}^2 tends to zero, χ_{ME} diverges. It worth noting, that the last formula for χ_{ME} is in agreement with that written in Ref. 8 allowing for $\gamma_{22}/2\sqrt{\beta_{11}\alpha_{11}}<1$, as follows from the FEM phase stability (see Table I).

The coefficients α_1 and β_1 are temperature and radius dependent. They can be rewritten as $\alpha_1=\alpha_T[T-T_{ce}(R)]$ and $\beta_1=\beta_T[T-T_{cm}(R)]$. Substituting them into Eqs. (19)–(21), we obtained

$$\chi_E = \frac{C_E}{(T_{CE}^* - T)}, \tag{22}$$

$$\chi_M = \frac{C_M}{(T_{CM}^* - T)}, \tag{23}$$

$$\chi_{ME} = \frac{\gamma_{22}}{2\sqrt{\alpha_{11}\beta_{11}}}\sqrt{\frac{C_EC_M}{(T_{CT}^* - T)(T_{CM}^* - T)}}. \tag{24}$$

Here, we introduced temperatures and Curie-Weiss constants renormalized by the magnetoelectric interaction,

$$T_{CE}^* = \frac{2\beta_{11}\alpha_T T_{cl}(R) - \beta_T\gamma_{22}T_{cm}(R)}{2\beta_{11}\alpha_T - \beta_T\gamma_{22}}, \tag{25a}$$

TABLE II. The boundaries between different phases (if any) in the absence of external fields.

Transition	Order	Condition
PP-FE	II	$\alpha_1=0$ [i.e., $T=T_{ce}(R)$]
PP-FM	II	$\beta_1=0$ [i.e., $T=T_{cm}(R)$]
FE-FM	I	$\alpha_1^2/\alpha_{11}=\beta_1^2/\beta_{11}$
FE-FEM	II	$\alpha_1\gamma_{22}=2\beta_1\alpha_{11}$ {i.e., $T=T_{cm}(R)-[\gamma_{22}(R)/\beta_T]P_3^2(T,R)$}
FM-FEM	II	$\beta_1\gamma_{22}=2\alpha_1\beta_{11}$ {i.e., $T=T_{ce}(R)-[\gamma_{22}(R)/\alpha_T]M_1^2(T,R)$}

$$T^*_{CM}=\frac{2\alpha_{11}\beta_T T_{cm}(R)-\alpha_T\gamma_{22}T_{cl}(R)}{2\alpha_{11}\beta_T-\alpha_T\gamma_{22}}, \tag{25b}$$

$$C_E=\frac{\beta_{11}}{2(2\alpha_T\beta_{11}-\beta_T\gamma_{22})}, \quad C_M=\frac{\alpha_{11}}{2(2\alpha_{11}\beta_T-\alpha_T\gamma_{22})}. \tag{26}$$

It is easy to see that Eq. (18) can be rewritten as

$$P^2_{FEM}=A_E(T^*_{CE}-T), \tag{27a}$$

$$M^2_{FEM}=A_M(T^*_{CM}-T), \tag{27b}$$

$$A_E=\frac{2\alpha_T\beta_{11}-\beta_T\gamma_{22}}{4\alpha_{11}\beta_{11}-\gamma_{22}^2}, \quad A_M=\frac{2\alpha_{11}\beta_T-\alpha_T\gamma_{22}}{4\alpha_{11}\beta_{11}-\gamma_{22}^2}. \tag{28}$$

Therefore, we obtained the conventional formula for order parameters and susceptibilities renormalized by size effect and magnetoelectric coupling transition temperatures and all the coefficients. Note that the case of the FE or FM phase can be obtained from Eqs. (22)–(28) at the limit $\gamma_{22}\to 0$.

In what follows, we will consider the property behavior in a broad temperature region with different phases. Therefore, it is necessary to consider first phase diagrams, allowing for their dependence on ME coupling value and radius of nanorods.

Since the free energy [Eq. (12)] renormalized coefficients [Eqs. (6), (7), and (9)] depend on the rod radius, Table I allows one to construct phase diagrams in different coordinates. As one can see from the table, there are no ranges of coexistence between PP and (FE, FM) phases or FEM and (FE, FM, PP) phases. At the same time, there is some possibility for FE and FM phases to coexist. In this case, the phase transition between FE and FM would be of the first order. The phase transition between other phases (PP with FE or FM, or FEM with FE or FM or PP) is of the second order. The conditions of the phase transitions are summarized in the Table II.

The last two rows of Table II proved that the quadratic magnetoelectric coupling term $\gamma_{22}M_1^2P_3^2$ acts as a secondary ferroic phase suppressing or enhancing factor depending on γ_{22} sign. Positive γ_{22} values decrease the phase transition temperature, while the negative ones increase it.

We predict that high enough ME coupling $[\gamma_{22}(R)<0, |\gamma_{22}(R)|\geqslant\gamma_{22}^b]$ may lead to the condition $\beta_1(T)+\gamma_{22}P_3^2\leqslant 0$ in some temperature range even at $\beta_1(T=0)\geqslant 0$ and thus may induce a ferromagnetic phase in small nanorods even if this phase is absent in bulk materials (similar to the appearance of ferroelectricity in incipient ferroelectric nanorods[22]). In order to demonstrate such a situation, below, we consider the case of $T^b_{cm}=0$, $T^b_{ce}=0$ (i.e., when the bulk material has no ferroic properties, so it can be a PP phase only at large radius). For the case, one should introduce the ferroelectric to ferromagnetic energy ratio $W=\sqrt{\alpha_{11}/\beta_{11}}$ and dimensionless quadratic magnetoelectric coupling coefficient $\Gamma_{22}(R)=\gamma_{22}(R)/\sqrt{4\alpha_{11}\beta_{11}}$. Phase diagrams for the case of $T^b_{cm}=0$, $T^b_{ce}=0$ and different values of R_Z, Γ^b_{22}, and β_T/α_T are shown in Fig. 4 for the typical case $\beta_T/\alpha_T=10^2$ because for the majority of ferroic materials, $\beta_T/\alpha_T\gg 1$ (the cases $\beta_T/\alpha_T=1$ and $\beta_T/\alpha_T=10^{-2}$ are considered in Ref. 36). In the case $T^b_{cm}=0$, $T^b_{ce}=0$, ferroic phase appears at small radii and the transition temperatures increase with radius decrease. As seen from Fig. 4, the region of the FEM phase existence is wider for the case $\Gamma_{22}<0$ than for $\Gamma_{22}>0$ [compare plots (a) and (c) with (b) and (d)] as anticipated. The ratio R_Z/R_Q increase stimulates the FEM and FM phase appearance [compare plots (a) and (b) with (c) and (d)].

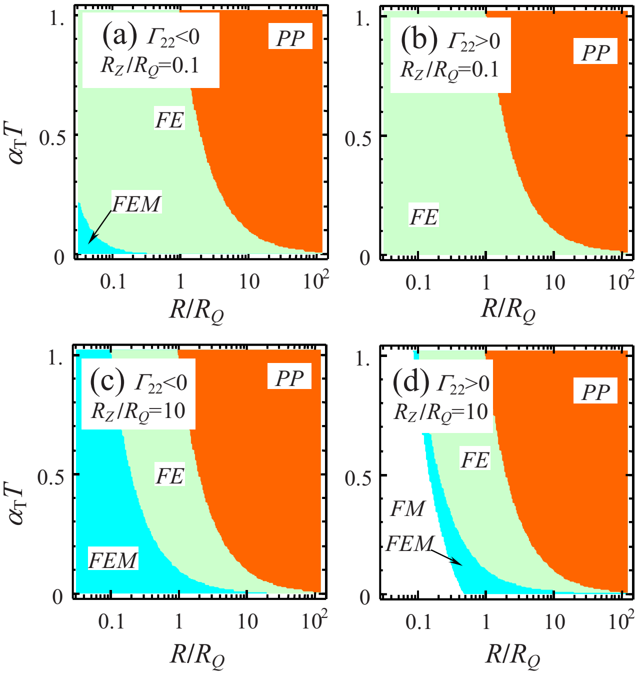

FIG. 4. (Color online) Phase diagrams for the following parameters: $\beta_T/\alpha_T=10^2$, $T^b_{cm}=0$, $T^b_{ce}=0$, $\sqrt{\alpha_{11}/\beta_{11}}=1.5$, $R_Q>0$, $R_{22}/R_Q=30$, $\rho_{A,B}=0$, $H_0=0$, and $E_0=0$. (a) $\Gamma^b_{22}=-10^{-3}$, $R_Z/R_Q=0.1$; (b) $\Gamma^b_{22}=10^{-3}$, $R_Z/R_Q=0.1$; (c) $\Gamma^b_{22}=-10^{-3}$, $R_Z/R_Q=10$; (d) $\Gamma^b_{22}=10^{-3}$, $R_Z/R_Q=10$.

Phase diagrams of the considered system for different nonzero ratios T^b_{cm}/T^b_{ce} are presented in Fig. 5.

Comparing Fig. 5(a) with Fig. 5(b), one can see that the increase of T^b_{cm}/T^b_{ce} ratio drastically changes the phase sequence and existence, namely, FE phase disappears and FM and FEM phase regions essentially increase for $T^b_{cm}/T^b_{ce}=1$ in comparison with the case $T^b_{cm}/T^b_{ce}=0.1$. The region of several phase coexistence is denoted by a circle in Fig. 5(a).

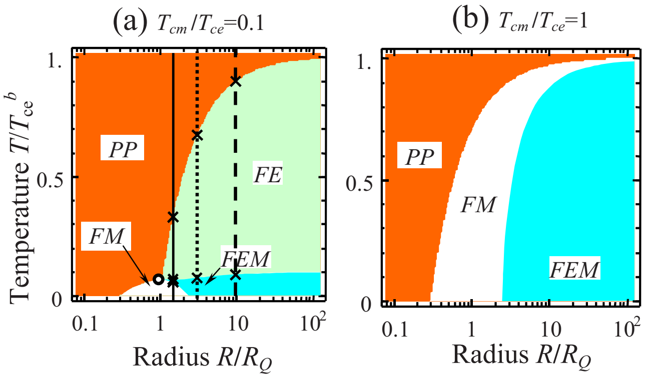

FIG. 5. (Color online) Phase diagrams for parameters $\Gamma_{22}^b=10^{-2}$, $(\beta_T T_{cm}^b\sqrt{\alpha_{11}})/(\alpha_T T_{ce}^b\sqrt{\beta_{11}})=1.5$, $R_Q>0$, $R_Q/R_{22}=10^{-2}\alpha_T T_{ce}^b$, $R_Z/R_Q=0.3\beta_T T_{cm}^b/\alpha_T T_{ce}^b$, $\rho_{A,B}=0$, $H_0=0$, and $E_0=0$. (a) $T_{cm}^b/T_{ce}^b=0.1$ and (b) $T_{cm}^b/T_{ce}^b=1$.

Figures 6(a) and 6(b) demonstrate the temperature dependencies of polarization and magnetization at zero fields and different nanorod radii. It is seen that the onset of magnetization leads to the appearance of the polarization curve fracture, though it is very weak for bulk systems due to the weak ME coupling. Additional fracture and/or break can be seen on the temperature dependence of linear dielectric susceptibility [Fig. 6(c)].

The corresponding temperatures of phase transitions can be determined from crossings of the vertical lines with phase boundaries on the diagram [Fig. 5(a)], namely, the divergence of χ_E [Fig. 6(c)] takes place in the points denoted by crosses in Fig. 5(a). It is clear that for the large radius, the temperature dependencies are almost the same as in the bulk material with transition temperatures T_{ce}^b and T_{cm}^b (see dash-dotted curves). With radius decrease, the ME coupling coefficient $\Gamma_{22}(R)$ increases in accordance with Eq. (11). The transition between FE and FEM phases via ME effect causes the small fracture on the ferroelectric order parameter curve at the temperature $T<T_{cm}^b$ of magnetization M_1 appearance [see Figs. 6(a) and 6(b)] that is close to T_{cm}^b [see dashed curves and dashed line in Figs. 6(a) and 5(a)]. With further radius decrease, ME coupling also increases (i.e., the term $\Gamma_{22}M_1^2$ increases) and so the fracture on the order parameter curves becomes much more pronounced and slightly shifts to the lower temperatures; it also appears on the susceptibility curve [see dotted curves in Fig. 6(c) and dotted line in Fig. 5(a) indicating FE to FM transition]. The shift from the bulk transition temperature T_{cm}^e is related to α_1 renormalization given by Eq. (13a). The shift increases with radius decrease. Finally, at small enough nanorod radius and positive $\Gamma_{22}(R)$ value, ME coupling suppresses the polarization and thus induces the transition from FEM to FM phase at temperatures $T<T_{cm}^b$ [see solid curve in Fig. 6(a) and solid line in Fig. 5(a)]. Appearance of phase transition leads to the additional low temperature divergence of the dielectric susceptibility [see solid curve in Fig. 6(c)]. The ME coupling-induced ferroelectric-paraelectric phase transition appeared under the condition $\alpha_1+\gamma_{22}M_1^2\geqslant 0$.

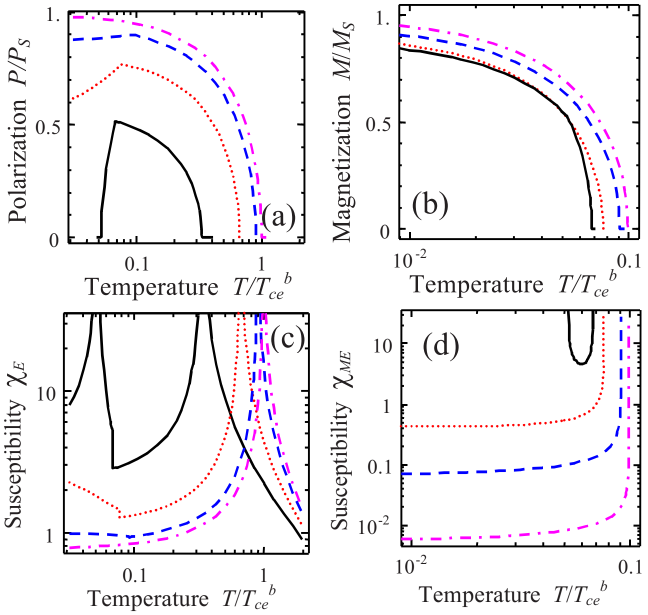

FIG. 6. (Color online) Temperature dependence of (a) polarization P_3, (b) magnetization M_1, (c) dielectric susceptibility χ_E, and (d) magnetoelectric susceptibility χ_{ME} at zero electric field for different nanorod radii $R/R_Q=1.5$, 3, 10, and 10^3 (solid, dotted, dashed, and dash-dotted curves) and the same other material parameters as in Fig. 5(a).

The magnetoelectric susceptibility χ_{ME} [Fig. 6(d)] is different from zero only in the ranges where both the polarization and magnetization are present. It diverges near the points where one of the order parameters tends to zero [see Eq. (24)]. In particular, dotted, dashed, and dash-dotted curve divergences originated from magnetization appearance. Additional divergence on solid curve in Fig. 6(d) is related to ME coupling-induced polarization disappearance [see solid curve in Fig. 6(a)]. It is seen from Fig. 6(d) that the decrease of radius leads to the increase of the magnetoelectric susceptibility.

C. Phase diagrams, polarization, dielectric susceptibility, and magnetoelectric susceptibility under external fields

The application of magnetic field to a multiferroic nanomaterial with high ME coupling opens the way to govern not only its magnetic properties but also the electric ones, which are extremely important for the majority of the material applications.

The application of electric or magnetic field induces the corresponding order parameter (polarization or magnetization), so that formally paraphase could not be introduced. At the same time, mixed phase FEM could exist. Typically, two limiting cases $E_0=0$, $H_0\neq 0$ and $E_0\neq 0$, $H_0=0$ have been considered.

(a) In the absence of electric field ($E_0=0$), the system under magnetic field could be either in FM or in FEM phases. For the case $4\alpha_{11}\beta_{11}-\gamma_{22}^2>0$, $\beta_1\gamma_{22}-2\alpha_1\beta_{11}>0$, $\alpha_1<0$, FEM is stable only for the magnetic fields $H_0<H_I$, where H_I is the first critical magnetic field. For the fields above the critical value $H_0>H_I$, FEM phase transforms into the FM one. The critical value of the field can be written as

$$H_I = 2\sqrt{-\frac{\alpha_1}{\gamma_{22}}}\left(\beta_1 - 2\frac{\alpha_1}{\gamma_{22}}\beta_{11}\right). \tag{29}$$

For the case $4\alpha_{11}\beta_{11}-\gamma_{22}^2<0$, FEM phase is stable only at $H_0>H_{II}$, where the second critical value of the field can be written as

$$H_{II} = \frac{2}{3}\sqrt{\frac{\alpha_1\gamma_{22}-2\beta_1\alpha_{11}}{3(4\alpha_{11}\beta_{11}-\gamma_{22}^2)}}\left(2\beta_1 - \frac{\gamma_{22}}{\alpha_{11}}\alpha_1\right). \tag{30}$$

In the region where the first order phase transition takes place, both expressions (29) and (30) make sense and there is hysteresis for the fields $H_I<H_0<H_{II}$.

(b) In the absence of magnetic field ($H_0=0$), the system under electric field could be in either in the FE or FEM phases. For the case $4\alpha_{11}\beta_{11}-\gamma_{22}^2>0$, $\alpha_1\gamma_{22}-2\beta_1\alpha_{11}>0$, $\beta_1<0$, FEM is stable only for the fields $E_0<E_I$, and for the field above critical value E_I, FEM phase transforms into the FE one,

$$E_I = 2\sqrt{-\frac{\beta_1}{\gamma_{22}}}\left(\alpha_1 - 2\frac{\beta_1}{\gamma_{22}}\alpha_{11}\right). \tag{31}$$

For the case $4\alpha_{11}\beta_{11}-\gamma_{22}^2<0$, FEM phase is stable only at $E_0>E_{II}$, where the critical value of the field can be written as

$$E_{II} = \frac{2}{3}\sqrt{\frac{\beta_1\gamma_{22}-2\alpha_1\beta_{11}}{3(4\alpha_{11}\beta_{11}-\gamma_{22}^2)}}\left(2\alpha_1 - \frac{\gamma_{22}}{\beta_{11}}\beta_1\right). \tag{32}$$

For the region where the first order phase transition takes place, both expressions (31) and (32) make sense and there is hysteresis for the fields $E_I<E_0<E_{II}$.

Using expressions (29) and (32), one can consider how the typical zero-field phase diagram from Fig. 5 changes under the presence of external fields, as presented in Fig. 7 for the cases of electric and magnetic fields respectively. There, we introduce normalized electric and magnetic fields $\tilde{E}=E_0/E_C$ and $\tilde{H}=H_0/H_C$, respectively, where the values $E_C=2\alpha_T T_{ce}^b P_S$ and $H_C=2\beta_T T_{cm}^b M_S$ are proportional to the thermodynamic coercive fields.

Under the field increase, the region of FEM phase existence is narrowed (compare curve 1 with 4 in Fig. 7), i.e., corresponding transition and/or stability limit temperatures shift to lower values.

Ferroelectric order parameter P_3 is shown in Fig. 8(a) at zero electric field $E=0$ and increasing magnetic field H_0 (in coercive field units) for positive coupling coefficient $\Gamma_{22}(R)>0$ and two values of nanorod radius (curve 1 for $R/R_Q=10$ and curve 2 for $R/R_Q=3$). The temperature dependence of susceptibilities χ_E and χ_{ME} are presented in Figs. 8(b) and 8(c), respectively. The temperature dependence of dielectric tunability $\delta\chi_E=[\chi_E(H)-\chi_E(0)]/\chi_E(0)$ is shown in Fig. 8(d). Corresponding phase changes can be determined from the dashed ($R/R_Q=10$) and dotted ($R/R_Q=3$) vertical lines on the phase diagram in Fig. 7(b).

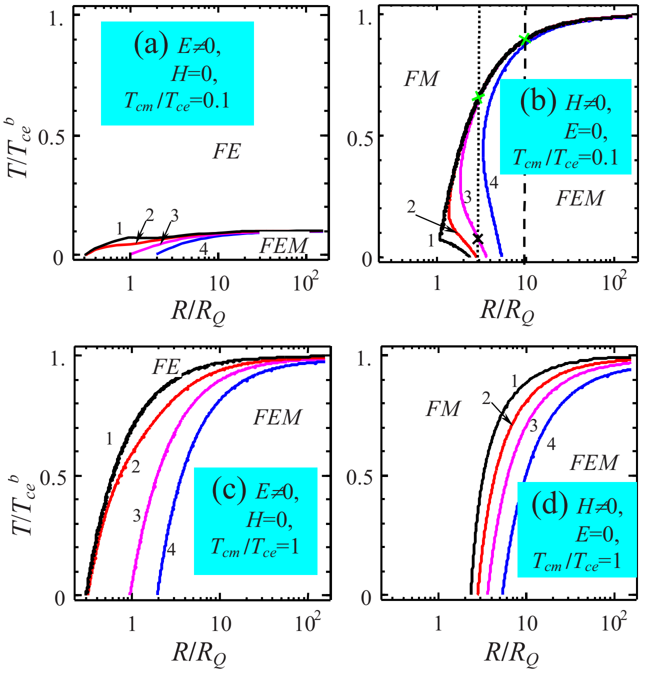

FIG. 7. (Color online) Phase diagrams for parameters $\Gamma_{22}^b=10^{-2}$, $(\beta_T T_{cm}^b\sqrt{\alpha_{11}})/(\alpha_T T_{ce}^b\sqrt{\beta_{11}})=1.5$, $R_Q>0$, $R_Q/R_{22}=10^{-2}\alpha_T T_{ce}^b$, $R_Z/R_Q=0.3\beta_T T_{cm}^b/\alpha_T T_{ce}^b$, and $\rho_{A,B}=0$. (a) $T_{cm}^b/T_{ce}^b=0.1$, $\tilde{H}=0$, $\tilde{E}=10^{-4}$, 0.3, 1, and 3 (curves 1, 2, 3, and 4); (b) $T_{cm}^b/T_{ce}^b=0.1$, $\tilde{H}=10^{-4}$, 0.3, 1, and 3, $\tilde{E}=0$ (curves 1, 2, 3, and 4); (c) $T_{cm}^b/T_{ce}^b=1$, $\tilde{H}=0$, $\tilde{E}=10^{-4}$, 0.3, 1, and 3 (curves 1, 2, 3, and 4); (d) $T_{cm}^b/T_{ce}^b=1$, $\tilde{H}=10^{-4}$, 0.3, 1, and 3, $\tilde{E}=0$ (curves 1, 2, 3, and 4).

It is clear from Fig. 8(a) that ferroelectric order parameter decreases and the phase transition at low temperature (see fractures on solid curves) smears with the magnetic field increase. The decrease is especially strong for small radius [compare curves 1 and 2, see comments to Fig. 6(a)]. High enough magnetic field due to ME coupling can induce the disappearance of ferroelectric polarization, which takes place under the condition $\alpha_1+\gamma_{22}M_1^2\geqslant 0$, i.e., when positive coupling term $\gamma_{22}M_1^2P_3^2$ suppresses the ferroelectric phase, as shown for curve 2. Additional calculations show that no such ferroelectric-ferromagnetic phase transition is observed at negative γ_{22}. At the same time, the shift of ferroelectric-paraelectric transition temperature is small.

It is seen from Fig. 8(b) that dielectric susceptibility χ_E increases with H_0 increase, as it should be expected from polarization decrease. At the same time, susceptibility break and fracture, seen at zero field (solid curves), smear at nonzero magnetic field. Additional divergence at dashed curve 2 corresponds to the polarization disappearance at low temperatures.

It is clear from Fig. 8(c) that magnetoelectric susceptibility χ_{ME} diverges in the point of FEM-FE phase transition at zero magnetic field (see solid curves). With magnetic field increase, the divergence diffuses into a maximum and then almost disappears (see dashed and dotted curves 1). Appearance of high temperature divergence is related to the phase transition between FEM and FM phases [see crosses in the intersections of dotted and dashed lines with solid curves in Fig. 7(b)]. Appearance of additional low temperature divergence for the case of small radii is related to two transition points FM-FEM and FEM-FM (see dashed curve 2). These transitions are marked by the crosses in the intersections of dotted line with solid curves in Fig. 7(b).

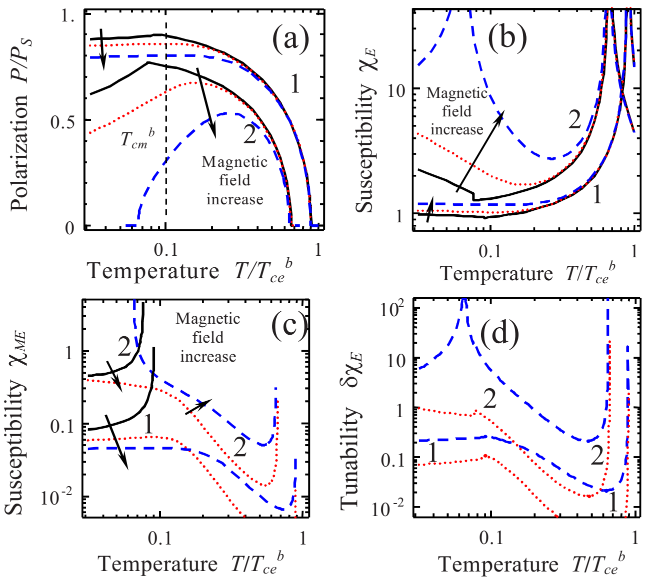

FIG. 8. (Color online) Temperature dependence of (a) polarization P_3, (b) dielectric susceptibility χ_E, (c) magnetoelectric susceptibility χ_{ME}, and (d) dielectric tunability $\delta\chi_E$ at zero electric field and different magnetic field values: H_0/H_C=0, 0.3, and 1 (solid, dotted, and dashed curves); relatively large nanorod radius R/R_Q =10 (curves 1) and small one R/R_Q=3 (curves 2) and the same other material parameters as in Fig. 7(b).

Therefore, anomalies of χ_{ME} behavior in the external field may obey the same law as that for the case of zero field, i.e., $\chi_{ME} < \sqrt{\chi_E \chi_M}$ (see Ref. 21), allowing for more general conditions of its validity (see Ref. 1).

It follows from Fig. 8(d) that the dielectric tunability increases under the magnetic field increase. Giant tunability appearance at small nanorod radius is caused by the ME coupling-induced FEM-FM phase transition taken place at positive γ_{22} values [see divergence in Fig. 6(d)]. Narrow divergences of tunability at higher temperatures are related with the weak dependencies of the susceptibility high temperature peaks on the magnetic field [see Fig. 8(b)]. The dielectric tunability is colossal (up to ten times and higher) in the vicinity of the phase transitions (compare with 500% effect shown in Fig. 2 from Ref. 13). These effects are absent in the bulk material, allowing for negligibly small bulk ME coupling coefficients.

VI. CONCLUSION

We predict the effects related with the renormalization of the magnetoelectric coupling coefficients caused by intrinsic surface stress in ferroic nanorods. The linear coupling coefficient is radius independent, whereas the quadratic ones include terms inversely proportional to the nanorod radius and thus strongly increase with radius decrease. We show the possibility to induce polarization and magnetization as well as magnetoelectric coupling by the surface stress in the nanorods of materials nonferroelectric and nonferromagnetic in bulk.

The renormalized magnetoelectric effect increases the relative dielectric tunability 3–50 times. At small magnetic field, the magnetoelectric tunability increases under the magnetic field increase. A jump of the relative dielectric tunability is related to the ferromagnetic phase transition shifted by the ME coupling. The jump height increases with magnetic field increase. Giant tunability (more than 40 times) appearance at high enough magnetic fields is caused by the ME coupling-induced ferroelectric-paraelectric phase transition taken place at positive coupling coefficient.

The quadratic magnetoelectric coupling dramatically changes the phase diagrams of ferroic nanorods with their radius decrease. ME coupling-induced ferroelectric-paraelectric phase transition (absent in the bulk) takes place at high enough magnetic fields. The transition appeared at positive coupling coefficients, when the magnetoelectric effect suppresses the ferroelectric phase. Also, the second order phase transition may become a first one.

The intrinsic surface stress under the curved nanorod surface shifts the ferroelectric and ferromagnetic transition temperatures. The corresponding transition temperature shift (unrelated with ME effect) may induce ferromagnetism in small nanorods absent in the bulk material. Similar mechanism could explain the recently observed room temperature ferromagnetism in small nanoparticles of nonmagnetic oxides.

Under the presence of piezomagnetic and piezoelectric effects, the intrinsic surface stress induces built-in magnetic and electric fields correspondingly. Built-in fields are inversely proportional to the nanorod radius. The fields smear magnetic, dielectric, and magnetoelectric susceptibility temperature maxima as well as increase their values in the paraphase. Built-in fields may overcome the coercive fields and thus essentially increase dielectric tunability even in the absence of external fields.

ACKNOWLEDGMENT

This work was supported in part by MULTICERAL.

---

*Corresponding author. Permanent address: V. Lashkarev Institute of Semiconductor Physics, NAS of Ukraine, 41, Pr. Nauki, 03028 Kiev, Ukraine. morozo@i.com.ua

[1] J. F. Scott, Nat. Mater. **6**, 256 (2007).
[2] P. Curie, J. Phys. (Paris), Colloq. **3**, 393 (1894).
[3] D. N. Astrov, Sov. Phys. JETP **11**, 708 (1960).
[4] V. K. Wadhawan, *Introduction to Ferroic Materials* (Gordon and Breach, New York, 2000).
[5] E. Roduner, *Nanoscopic Materials: Size-dependent Phenomena* (RSC, Cambridge, 2006).
[6] Michael G. Cottan, *Linear and Nonlinear Spin Waves in Magnetic Films and Super-lattices* (World Scientific, Singapore, 1994).

[7] R. Ramesh and N. A. Spaldin, Nat. Mater. **6**, 21 (2007).

[8] M. Fiebig, J. Phys. D **38**, R123 (2005).

[9] Ce Wen Nan, Phys. Rev. B **50**, 6082 (1994).

[10] Ce Wen Nan, Ming Li, and Jin H. Huang, Phys. Rev. B **63**, 144415 (2001).

[11] S. Dong, J. F. Li, and D. Viehland, Philos. Mag. **83**, p.769 (2003).

[12] J. X. Zhang, Y. L. Li, D. G. Schlom, L. Q. Chen, F. Zavaliche, R. Ramesh, and Q. X. Jia, Appl. Phys. Lett. **90**, 052909 (2007).

[13] J. Hemberger, P. Lunkenheimer, R. Fichtl, H.-A. Krug von Nidda, V. Tsurkan, and A. Loidl, Nature (London) **434**, 364 (2005).

[14] H. Katsura, N. Nagaosa, and A. V. Balatsky, Phys. Rev. Lett. **95**, 057205 (2005).

[15] P. Bruno and V. K. Dugaev, Phys. Rev. B **72**, 241302(R) (2005).

[16] M. I. Bichurin, V. M. Petrov, Yu. V. Kiliba, and G. Srinivasan, Phys. Rev. B **66**, 134404 (2002).

[17] G. A. Smolenskii and L. I. Chupis, Sov. Phys. Usp. **25**, 475 (1982).

[18] J. Wang, J. B. Neaton, H. Zheng, V. Nagarajan, S. B. Ogale, B. Liu, D. Viehland, V. Vaithyanathan, D. G. Schlom, U. V. Waghmare, N. A. Spaldin, K. M. Rabe, M. Wuttig, and R. Ramesh, Science **299**, 1719 (2003).

[19] B. Ruette, S. Zvyagin, A. P. Pyatakov, A. Bush, J. F. Li, V. I. Belotelov, A. K. Zvezdin, and D. Viehland, Phys. Rev. B **69**, 064114 (2004).

[20] A. Sundaresan, R. Bhargavi, N. Rangarajan, U. Siddesh, and C. N. R. Rao, Phys. Rev. B **74**, 161306(R) (2006).

[21] Y. Nakae, Y. Seino, T. Teranishi, M. Miyake, S. Yamada, and H. Hori, Physica B **284-288**, 1758 (2000).

[22] A. N. Morozovska, M. D. Glinchuk, and E. A. Eliseev, Phys. Rev. B **76**, 014102 (2007).

[23] E. A. Eliseev, M. D. Glinchuk, and A. N. Morozovska, Phys. Status Solidi B **244**, 3660 (2007).

[24] M. D. Glinchuk, E. A. Eliseev, V. A. Stephanovich, and R. Farhi, J. Appl. Phys. **93**, 1150 (2003).

[25] M. D. Glinchuk and A. N. Morozovska, Phys. Status Solidi B **238**, 81 (2003).

[26] J. S. Speck and W. Pompe, J. Appl. Phys. **76**, 466 (1994).

[27] M. D. Glinchuk, A. N. Morozovska, A. M. Slipenyuk, and I. P. Bykov, Appl. Magn. Reson. **24**, 333 (2003).

[28] M. D. Glinchuk, I. V. Kondakova, V. V. Laguta, A. M. Slipenyuk, I. P. Bykov, A. V. Ragulya, and V. P. Klimenko, Acta Phys. Pol. A **108**, 47 (2005); A. M. Slipenyuk, I. V. Kondakova, M. D. Glinchuk, and V. V. Laguta, Phys. Status Solidi (RRL) **4**, 1297 (2007).

[29] L. D. Landau and E. M. Lifshitz, *Electrodynamics of Continuous Media* (Butterworth-Heinemann, Oxford, 1980).

[30] L. D. Landau and E. M. Lifshitz, *Theory of Elasticity. Theoretical Physics* (Butterworth-Heinemann, Oxford, 1998), Vol. 7.

[31] V. I. Marchenko and A. Ya. Parshin, Zh. Eksp. Teor. Fiz. **79**, 257 (1980) [Sov. Phys. JETP **52**, 129 (1980)].

[32] V. A. Shchukin and D. Bimberg, Rev. Mod. Phys. **71**, 1125 (1999).

[33] M. D. Glinchuk and A. N. Morozovska, J. Phys.: Condens. Matter **16**, 3517 (2004).

[34] M. D. Glinchuk, A. N. Morozovska, and E. A. Eliseev, J. Appl. Phys. **99**, 114102 (2006).

[35] *Encyclopedia: Solid State Physics* (Naukova Dumka, Kiev, 1996), Pt. I, p. 501. In SI units. $H_p(R)=(s_{12}/s_{11})g^m_{13}(4\mu/\mu_0 R)$, $B=\chi_r\mu_0 H$, and $\chi_r\cong 10^3$.

[36] M. D. Glinchuk, E. A. Eliseev, A. N. Morozovska, and R. Blinc, arXiv:0709.3058 (unpublished).

[37] W. Ma, M. Zhang, and Z. Lu, Phys. Status Solidi A **166**, 811 (1998).